

Multifrequency superscattering pattern shaping

Yao Qin (秦瑶)¹, Jinying Xu (徐金英)², Yineng Liu (刘益能)^{1*}, and Huanyang Chen (陈焕阳)¹

¹Institute of Electromagnetics and Acoustics and School of Electronic Science and Engineering, Xiamen University, Xiamen 361005, China

²Department of Physics, Fuzhou University, Fuzhou 350108, China

*Corresponding author: lyn610@xmu.edu.cn

Received March 17, 2021 | Accepted May 14, 2021 | Posted Online September 1, 2021

Multifrequency superscattering is a phenomenon in which the scattering cross section from a subwavelength object simultaneously exceeds the single-channel limit at multiple frequency regimes. Here, we achieve simultaneously, within a graphene-coated subwavelength structure, multifrequency superscattering and superscattering shaping with different engineered scattering patterns. It is shown that multimode degenerate resonances at multiple frequency regimes appearing in a graphene composite structure due to the peculiar dispersion can be employed to resonantly overlap electric and magnetic multipoles of various orders, and, as a result, effective multifrequency superscattering with different engineered angular patterns can be obtained. Moreover, the phenomena of multifrequency superscattering have a high tolerance to material losses and some structural variations. Our work should anticipate extensive applications ranging from emission enhancing, energy harvesting, and antenna design with improved sensitivity and accuracy due to multifrequency operation.

Keywords: superscattering pattern shaping; subwavelength structure; graphene; plasmon polariton.

DOI: [10.3788/COL202119.123601](https://doi.org/10.3788/COL202119.123601)

1. Introduction

In recent years, there have been many interests in studying electromagnetic superscattering because of its special applications^[1–11] in antenna design, optical sensing and detection, bioimaging, optical tagging to spectroscopy, scattering-particle-assisted passive radiation cooling, and photovoltaic devices. To realize superscattering for a subwavelength object, complementary metamaterials based on transformation optics have been proposed initially to drastically enhance the scattering cross section of a particle^[12,13]. This approach requires both electrical and magnetic anisotropic inhomogeneous parameters. In order to relax the requirement, Ruan and Fan proposed a subwavelength object with a plasmonic-dielectric-plasmonic layer structure, and numerically demonstrated that the total scattering cross section of a subwavelength structure could far exceed the single-channel limit when multiple plasmonic resonant modes were aligned^[14]. Later, many theoretical works have been performed to generate superscattering by various structures^[14–23]. Subwavelength multilayer structures have become widely used to overcome the single-channel limit by exciting degenerated confined waves, such as localized surface plasmons in metal^[14] or graphene^[15–17] and multipolar Mie resonances in anisotropic high index dielectrics^[18–20]. Recently, a low or near zero refractive index environment has been proposed as a novel mechanism to enhance the scattering from tiny objects, which has been proved in some works^[24,25].

All of the above-mentioned superscattering phenomena exhibit a single-frequency regime. Multifrequency superscattering may enable improved sensitivity and accuracy for extensive applications ranging from sensing, bioimaging, and optical tagging to spectroscopy^[26,27]. Only very recently was a multifrequency superscatterer first, to the best of our knowledge, proposed by using a subwavelength hyperbolic structure^[28]. Since then, multifrequency superscattering from a deep-subwavelength spoof plasmonic structure has been also discussed^[29]. Moreover, a subwavelength metasurface-based all-metal or metal dielectric structures with low material losses has also been proposed to experimentally achieve multifrequency superscattering by degenerate resonances of confined surface waves^[30,31]. Very recently, a graphene-based dual-band superscatterer at mid-infrared frequencies is proposed, and the phenomena of dual-band superscattering are tunable^[32]. However, the obtained multifrequency superscattering arises mainly from the constructive interference of scattering fields from different channels in the forward direction. In this paper, we have achieved simultaneously, within a graphene-based subwavelength structure, multifrequency superscattering and superscattering shaping with different engineered scattering patterns induced by the interferences of multipoles resonantly overlapped. Due to multiple polaritonic dispersion lines in a graphene-based subwavelength structure, the phenomena of multifrequency superscattering are found to have a high tolerance to some structural variations and realistic graphene loss.

In contrast with multilayer plasmonic structures, the performance of the proposed structure can be easily refined for the desired frequency by adjusting the chemical potential and loss of the graphene layer.

2. Theory

In this work, we consider a two-dimensional subwavelength cylindrical structure. The structure consists of six layers of dielectric material, each of which is coated with a graphene shell, as shown in Fig. 1(a). Such a six-layer subwavelength structure is the main focus of this analysis, because six layers is sufficient for multifrequency superscattering and superscattering shaping. The conductivity of graphene can be expressed as the Kubo formula: $\sigma_g(\omega, \mu_c, \tau, T) = \sigma_{\text{intra}} + \sigma_{\text{inter}}$ ^[17]. The TM-polarized plane wave with the wave vector k along the x direction and magnetic field along the z direction is incident from the left side of the cylinder structure. Based on the transfer matrix approach of multilayered cylindrical structures^[32–34], the incident and

scattered magnetic field in the outermost surrounding air region can be expressed as

$$\vec{H}_{\text{inc}} = \vec{z} H_0 \sum_{m=-\infty}^{\infty} i^m J_m(k_b \rho) e^{im\phi}, \quad (1)$$

$$\vec{H}_{\text{sca}} = \vec{z} H_0 \sum_{m=-\infty}^{\infty} i^m s_m H_m^{(1)}(k_b \rho) e^{im\phi}, \quad (2)$$

where H_0 is the amplitude of the incident field, ϕ and ρ are the azimuthal angle and radial component, respectively, and J_m and $H_m^{(1)}$ denote the Bessel function and the Hankel function of the first kind with order m , respectively. $k_b = \omega/c$ is the wavenumber in free space, and s_m is the scattering coefficient with the m th angular momentum channel. The magnetic field in the subwavelength cylindrical structure for $\rho_{n-1} < \rho < \rho_n$ ($n = 2, 3, \dots, 6$) and $\rho < \rho_1$ can be respectively written as

$$\vec{H}_n = \vec{z} H_0 \sum_{m=-\infty}^{+\infty} i^m [b_{m,n} J_m(k_n \rho) + c_{m,n} H_m^{(1)}(k_n \rho)] e^{im\phi}, \quad (3)$$

$$\vec{H}_1 = \vec{z} H_0 \sum_{m=-\infty}^{\infty} i^m a_m J_m(k_1 \rho) e^{im\phi}, \quad (4)$$

where ρ_1 is the radius of the innermost layer of the dielectric, $k_n = \omega/c\sqrt{\epsilon_n}$ is the wavenumber in the n th layer of the dielectric medium, and $b_{m,n}$, $c_{m,n}$, and a_m are the magnetic-field coefficients with order m . According to Maxwell's equation, the corresponding electric field can be calculated by $\vec{E} = \frac{i}{\omega\epsilon_0} \nabla \times \vec{H}$. The electric and magnetic field at the interface $\rho = \rho_i$ ($i = 1, 2, \dots, 6$) can be restrained by the following boundary conditions for the graphene shells between adjacent layers of dielectric^[35]:

$$\vec{n} \times (\vec{E}_{n+1,\phi} - \vec{E}_{n,\phi}) = 0, \quad (5)$$

$$\vec{n} \times (\vec{H}_{n+1,z} - \vec{H}_{n,z}) = \vec{J}. \quad (6)$$

Here, $J = \sigma(\omega)E_\phi$ is the surface current of graphene satisfying Ohm's law. To derive the scattering coefficient s_m , dynamical matrix $D_{m,n}$ and $M_{m,n+1}$ are defined as

$$D_{m,n}(\rho_n) = \begin{bmatrix} J_m(k_n \rho_n) & H_m^{(1)}(k_n \rho_n) \\ \frac{\sqrt{\epsilon_n} J'_m(k_n \rho_n)}{\epsilon_n} & \frac{\sqrt{\epsilon_n} H_m^{(1)'}(k_n \rho_n)}{\epsilon_n} \end{bmatrix}, \quad (7)$$

$$M_{m,n+1}(\rho_n) = \begin{bmatrix} J_m(k_{n+1} \rho_n) - i\sigma_n \eta_1 & H_m^{(1)}(k_{n+1} \rho_n) - i\sigma_n \eta_2 \\ \frac{\sqrt{\epsilon_{n+1}} J'_m(k_{n+1} \rho_n)}{\epsilon_{n+1}} & \frac{\sqrt{\epsilon_{n+1}} H_m^{(1)'}(k_{n+1} \rho_n)}{\epsilon_{n+1}} \end{bmatrix}, \quad (8)$$

where $\eta_1 = k_{n+1} J'_m(k_{n+1} \rho_n) / (\omega \epsilon_0 \epsilon_{n+1})$ and $\eta_2 = k_{n+1} H_m^{(1)'}(k_{n+1} \rho_n) / (\omega \epsilon_0 \epsilon_{n+1})$. By substituting Eqs. (3)–(6) into Eqs. (7)

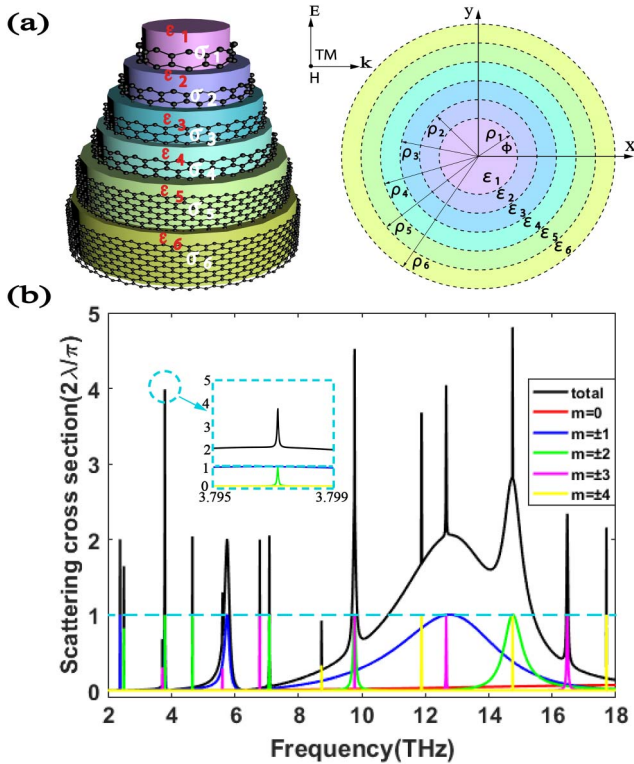


Fig. 1. (a) Illustration of a subwavelength multilayered cylindrical structure consisting of six layers of dielectric materials, each of which is coated with a graphene shell. Three-dimensional and two-dimensional views of the structure are shown in the left and right inset, respectively. Graphene shells are represented by black dotted lines. Here, the plane wave is TM-polarized and incident from the left side of the cylinder structure. (b) The scattering spectra (normalized scattering cross section) for the same structure in (a) under the ideal lossless assumption. Both the total scattering spectrum and the partial spectra of the first five scattering terms are shown. The inset in (b) shows the details at the resonance peak circled by a dotted blue line.

and (8), the coefficients $b_{m,n}$ and $c_{m,n}$ can be connected to $b_{m,n+1}$ and $c_{m,n+1}$ by the defined dynamical matrix $D_{m,n}$ and $M_{m,n+1}$ as follows:

$$D_{m,n}(\rho_n) \begin{bmatrix} b_{m,n} \\ c_{m,n} \end{bmatrix} = M_{m,n+1}(\rho_n) \begin{bmatrix} b_{m,n+1} \\ c_{m,n+1} \end{bmatrix}. \quad (9)$$

Then, from the recurrence relation of the coefficients of the adjacent layers, the relation between the coefficients of the innermost layer and the outermost layer can be described by the following formula:

$$\begin{bmatrix} J_m(k_1 \rho_1) & 0 \\ \frac{\sqrt{\epsilon_1} J'_m(k_1 \rho_1)}{\epsilon_1} & 0 \end{bmatrix} \begin{bmatrix} a_m \\ 0 \end{bmatrix} = T_m \begin{bmatrix} 1 \\ s_m \end{bmatrix}, \quad (10)$$

where

$$\begin{aligned} T_m &= M_{m,2}(\rho_1) \left\{ \prod_{n=2}^6 [D_{m,n}(\rho_n)]^{-1} \cdot M_{m,n+1}(\rho_n) \right\} \\ &= \begin{bmatrix} T_{m,11} & T_{m,12} \\ T_{m,21} & T_{m,22} \end{bmatrix}. \end{aligned} \quad (11)$$

Next, the scattering coefficient obtained according to Eqs. (12) and (13) can be expressed as

$$s_m = \frac{xT_{m,21} - yT_{m,11}}{yT_{m,12} - xT_{m,22}}, \quad (12)$$

where $x = J_m(k_1 \rho_1)$, $y = \sqrt{\epsilon_1} J'_m(k_1 \rho_1) / \epsilon_1$. Finally, the normalized scattering cross section (NSCS) can be calculated by

$$\text{NSCS} = \sum_{m=-\infty}^{+\infty} |s_m|^2. \quad (13)$$

Here, NSCS is normalized by $2\lambda/\pi$, where λ is the wavelength of the incident wave. According to the electromagnetic multipole analysis of a cylindrical structure^[20,36,37], for TM-polarized plane waves, s_0 , $s_{\pm 1}$, $s_{\pm 2}$, $s_{\pm 3}$, and $s_{\pm 4}$ correspond to the magnetic dipole (MD), electric dipole (ED), electric quadrupole (EQ), magnetic octupole (MO), and electric octupole (EO), respectively. Theoretically, the phenomenon of superscattering can be realized by making the NSCS exceed the single-channel limit. To enlarge the scattering cross section, material and geometrical parameters can be tuned so that different electromagnetic multipoles simultaneously appear at the same frequency. In this system, contributions of ED, EQ, MO, and EO are mainly considered because the contributions of other modes are so small that they could be ignored. Significantly, resonant overlapping of different multipoles can not only realize superscattering but also result in different scattering angular distributions.

3. Results and Discussions

To highlight the underlying physical properties, we first consider a lossless subwavelength cylindrical structure by setting $1/\tau \rightarrow 0$, where τ is the relaxation time of charge carriers of graphene. The scattering spectra (NSCS) as functions of the frequency for the structure in Fig. 1(a) are shown in Fig. 1(b). Both the total scattering spectrum and the partial spectra from channels with $m = 0$, $m = \pm 1$, $m = \pm 2$, $m = \pm 3$, and $m = \pm 4$ are plotted. The geometrical parameters are $\rho_1 = 1493$ nm and $d_n = \rho_n - \rho_{n-1} = 500$ nm ($n = 2, 3, \dots, 6$). Relative permittivities of dielectrics are $\epsilon_1 = 1.22$, $\epsilon_2 = 1.21$, $\epsilon_3 = 2.06$, $\epsilon_4 = 1.15$, $\epsilon_5 = 1.21$, and $\epsilon_6 = 2.3$. For all graphene shells, the chemical potential is $\mu_c = 0.72$ eV at temperature $T = 300$ K, and the thickness can be negligible. In the system, resonances from channels with $m = \pm 1$, $m = \pm 2$, $m = \pm 3$, and $m = \pm 4$ are mainly considered because the scattering cross sections from other channels are too small to be ignored. At 3.79715 THz, the total scattering cross section mostly comes from resonant channels with $m = \pm 1$ and $m = \pm 2$, and the scattering cross sections from these four channels almost all reach the signal-channel limit, which makes the total reach four times the signal-channel limit. The total scattering cross section at 9.77464 THz exceeds four times the signal-channel limit, which originates from a combination of the resonance peaks from channels with $m = \pm 2$ and $m = \pm 3$. Scattering cross sections of these peaks almost all reach signal-channel limit, and the contributions from channels with $m = \pm 1$ are negligible. Similarly, the resonance peaks at 12.65616 THz from channels with $m = \pm 1$ and $m = \pm 3$ are all nearly equal to the signal-channel limit, and they are overlapped well, which results in the total scattering cross section reaching four times the signal-channel limit. The resonance peaks with $m = \pm 2$ and $m = \pm 4$ are overlapped at 14.74908 THz, and these peaks are almost all equal to the signal-channel limit. Obviously, the contributions from channels with $m = \pm 1$ cannot be neglected, so the total scattering cross section is greater than four times the signal-channel limit at 14.74908 THz. This implies that multifrequency superscattering can be realized by overlapping electric and magnetic resonances with different orders.

The underlying mechanism of the resonant overlapping of multipoles in the subwavelength cylinder structure can be qualitatively understood from the dispersion of plasmon polaritons supported by a corresponding planar structure in Fig. 2. Starting from resonance modes supported in the corresponding planar structure, the resonances of the subwavelength cylinder structure can be understood using the whispering gallery condition based on the Bohr model^[14,17]. More specifically, the subwavelength cylinder supports the m th-order resonance at a frequency f , when the propagation constant β of all the modes for the corresponding planar structure satisfies the condition: $\beta 2\pi R_{\text{eff}} = 2\pi m$, where $R_{\text{eff}} = \sum_{i=1}^6 \rho_i / 6$ is the effective radius of the cylindrical structure. The dispersion curves of the equivalent planar structure are analyzed by the reflection pole method, which suggests that the surface modes of a layered medium are observed in the generalized reflection coefficient. It is performed after obtaining the scattering parameters from

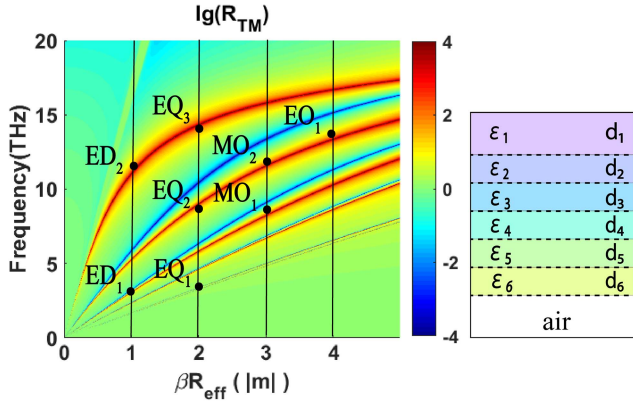


Fig. 2. Dispersion of plasmon polaritons versus $|R_{TM}|$ (in logarithmic scale) under the ideal lossless assumption is shown. R_{TM} is the reflection coefficient of the TM-polarized plane wave for the corresponding planar structure. The parameters of the corresponding planar structure are the same as those in Fig. 1(a), including the geometrical parameters $d_1 = 1493$ nm, $d_i = 500$ nm ($i = 2, 3, \dots, 6$) and material parameters $\epsilon_1 = 1.22$, $\epsilon_2 = 1.21$, $\epsilon_3 = 2.06$, $\epsilon_4 = 1.15$, $\epsilon_5 = 1.21$, and $\epsilon_6 = 2.3$. All of the graphene shells with $\mu_c = 0.72$ eV are represented by black dotted lines, the thickness of which can be negligible.

the transmission matrix^[32,38]. There are five branches in the dispersion lines due to the mode coupling of the graphene plasmons. Four black vertical solid lines $|m| = 1$, $|m| = 2$, $|m| = 3$, and $|m| = 4$ correspond to different modes ED, EQ, MO, and EO, respectively. Obviously, there are plenty of resonant frequencies of the multiple plasmonic modes in the dispersion lines. Here, only resonant frequencies with overlapped multipoles are analyzed. Two resonances at 3.79715 THz and 12.65616 THz from channel $|m| = 1$ are observed, and the positions of the corresponding resonance modes are marked by ED₁ and ED₂. Three resonances at 3.79715 THz, 9.77464 THz, and 14.74908 THz from channel $|m| = 2$ are observed, and the positions of the corresponding resonance modes are marked by EQ₁, EQ₂, and EQ₃. It is observed that a coincidence of ED₁ and EQ₁ at the frequency of 3.79715 THz interprets the combination of resonances from channels with $m = \pm 1$ and $m = \pm 2$ in Fig. 1(b). Two resonances at 9.77464 THz and 12.65616 THz from channel $|m| = 3$ are observed, and the positions of the corresponding resonance modes are marked by MO₁ and MO₂. It is clear that EQ₂ and MO₁ appear close to the frequency of 9.77464 THz, which interprets the combination of resonances from channels with $m = \pm 2$ and $m = \pm 3$ in Fig. 1(b). Similarly, resonances from channels with $m = \pm 1$ and $m = \pm 3$ can be overlapped at the frequency of 12.65616 THz because ED₂ and MO₂ appear close to the corresponding frequency. One resonance at 14.74908 THz from channel $|m| = 4$ is observed, and the position of the corresponding resonance mode is marked by EO₁. Clearly, EQ₃ and EO₁ appear close to the frequency of 14.74908 THz, and this means that the resonances from channels with $m = \pm 2$ and $m = \pm 4$ can be overlapped at the corresponding frequency. Therefore, multifrequency

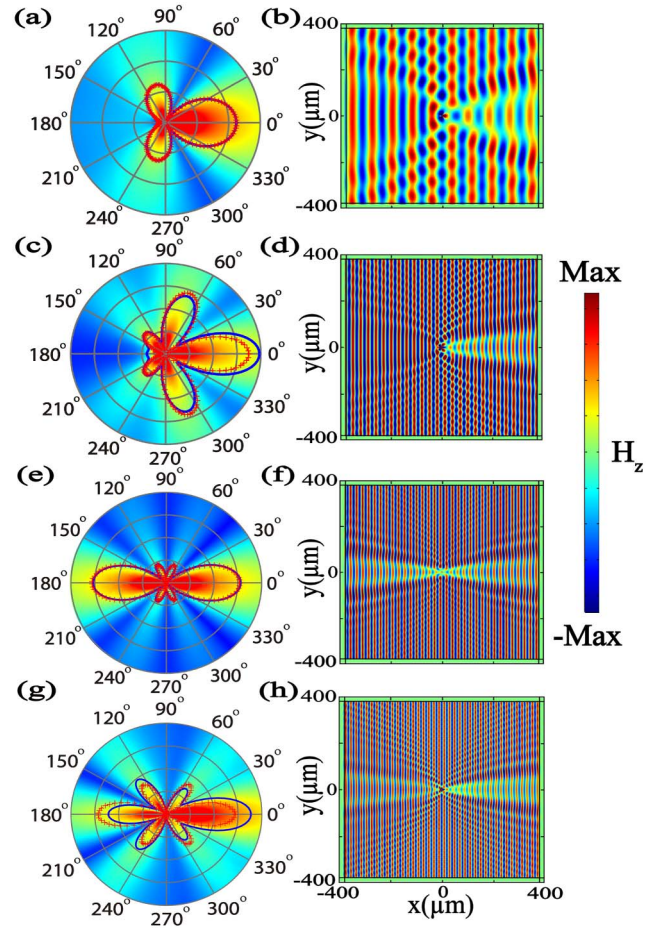


Fig. 3. Scattering angular distributions for the subwavelength cylinder structure in Fig. 1(a) at (a) 3.79715 THz, (c) 9.77464 THz, (e) 12.65616 THz, and (g) 14.74908 THz are shown, and the background patterns are the near fields $|H_z^{sca}|$ at the corresponding frequencies. The total scattering amplitudes are plotted by solid blue curves, and the ideal scattering patterns with solely overlapped (a) ED and EQ, (c) EQ and MO, (e) ED and MO, and (g) EQ and EO are plotted by red crosses. Total magnetic-field H_z distributions at the frequencies of (b) 3.79715 THz, (d) 9.77464 THz, (f) 12.65616 THz, and (h) 14.74908 THz are plotted.

superscattering with resonantly overlapped multipoles can be well understood through the dispersion lines.

Figure 3 intuitively shows the performance of the superscattering pattern shaping in the form of far and near fields for the cylinder structure in Fig. 1(a) at the four superscattering resonant frequencies. Far-field angular scattering amplitude $\Gamma(\phi)$ can be analyzed by the derived formula^[20]:

$$\Gamma(\phi) = \sqrt{2/\pi k} \left| s_0 + 2 \sum_{m=1}^{\infty} s_m \cos(m\phi) \right|. \quad (14)$$

Theoretically, various scattering pattern shaping can also be realized by resonantly overlapping different electromagnetic multipoles because these multipoles show different phase symmetries and parities^[20,39,40]. Specifically, the scatterings

exhibit opposite parities for multipoles of adjacent orders and the same nature (e.g., ED and EQ exhibit odd and even parity, respectively) or for multipoles of different natures but the same order (e.g., MD and ED exhibit even and odd parity, respectively).

Figure 3(a) shows the superscattering pattern shaping by resonantly overlapping ED and EQ at the resonant frequency of 3.79715 THz. Far-field scattering angular distribution is shown by a blue solid curve, and the scattering near field $|H_z^{\text{sca}}|$ is shown in the background pattern, which is in accord with the blue solid curve. As shown in Fig. 3(a), the scattering is enhanced in the forward direction but suppressed in the backward direction, because the scatterings of ED and EQ exhibit odd and even parities, respectively. The two multipoles are in phase in the forward direction and out of phase in the backward direction. In fact, in the forward direction, the two resonantly overlapped multipoles are always in phase according to the optical theorem^[20,41]. Additionally, the scattering is also enhanced from 90° to 135° and 225° to 270° in the backward half-scattering circle and suppressed from 45° to 90° and 270° to 315° in the forward half-scattering circle. This can be understood analytically by $\Gamma(\phi) \propto |\cos \phi + \cos(2\phi)|$ according to Eq. (16) with purely overlapping ED and EQ. The ideal scattering angular distribution with solely overlapped ED and EQ is plotted by red crosses, which is consistent with the blue solid curve from the contributions of other multipoles, except ED and EQ are so small that they can be neglected. For the near field, the total magnetic field H_z distribution at 3.79715 THz is shown in Fig. 3(b). The cylinder structure leaves a large “shadow” in the forward direction, and the size of the “shadow” in the forward direction is much larger than the diameter of the cylindrical structure. This arises from the fact that the radiated magnetic fields of resonantly overlapped multipoles interfere destructively with respect to the incident field in the forward direction, as is required by the optical theorem^[39,41]. Clearly, the near field H_z matches well with the scattering field in Fig. 3(a).

Figure 3(c) illustrates the superscattering pattern shaping with resonantly overlapped EQ and MO by showing the scattering-field distribution at the frequency of 9.77464 THz. The far-field scattering angular distribution is plotted by a blue solid curve, which matches well with the scattering near field shown in the background pattern. Like Fig. 3(a), the scattering is enhanced in the forward direction but suppressed in the backward direction due to opposite parities of EQ and MO (even and odd, respectively). The two overlapped multipoles are in phase and out of phase, respectively, in the forward and backward directions. It is observed that the scattering is also suppressed from 30° to 45° and 315° to 330° in the forward half-scattering circle, which can be understood analytically by $\Gamma(\phi) \propto |\cos(2\phi) + \cos(3\phi)|$ when EQ and MO are only overlapping. The red crosses plot the ideal scattering pattern with the two modes purely overlapped. The slight discrepancy between blue solid curve and red crosses originates from the fact that the contribution of the ED is negligible. For the near field, the total field H_z at 9.77464 THz is shown in Fig. 3(d). A remarkable “shadow” can also be seen in the forward direction, and the “shadow” is

much larger than the diameter of the cylindrical structure, which agrees well with the scattering field in Fig. 3(c).

Figure 3(e) illustrates the superscattering pattern shaping with resonantly overlapped ED and MO by showing the scattering-field distribution at the frequency of 12.65616 THz. The scattering near and far fields correspond to the background pattern and the blue solid curve, respectively, and they are well matched. Clearly, the scattering is enhanced symmetrically both in the forward and backward directions due to the same odd parity of the scatterings of ED and MO. Additionally, the interferences of overlapped ED and MO can also suppress the scattering at $\phi = 45^\circ$, $\phi = 90^\circ$, $\phi = 135^\circ$, $\phi = 225^\circ$, $\phi = 270^\circ$, and $\phi = 315^\circ$ due to $\Gamma(\phi) \propto |\cos \phi + \cos(3\phi)|$. When only considering the overlapped ED and MO, the ideal scattering angular distribution plotted by red crosses matches well with the blue solid curve because other contributions except for ED and MO are too small to be neglected. For the near field, the total magnetic field at the resonant frequency of 12.65616 THz is shown in Fig. 3(f), and the cylinder structure leaves a large “shadow” larger than the structure diameter, not only in the forward direction but also in backward direction, which is consistent with the scattering field in Fig. 3(e).

Figure 3(g) shows the superscattering pattern shaping by resonantly overlapping EQ and EO at the frequency of 14.74908 THz in the form of the scattering far field plotted by the blue solid curve and the scattering near field shown in the bottom pattern. The scattering amplitudes are symmetrically enhanced both in forward and backward directions, which is caused by the same even parity of the EQ and EO. It can be also seen that the scattering is suppressed from 22.5° to 45°, 67.5° to 112.5°, 135° to 157.5°, 202.5° to 225°, 247.5° to 292.5°, and 315° to 337.5° according to $\Gamma(\phi) \propto |\cos(2\phi) + \cos(4\phi)|$. The ideal scattering pattern with purely overlapped ED and EO plotted by red crosses does not coincide well with the blue solid curve because the contribution of the ED cannot be neglected at the frequency of 14.74908 THz. For the near field, at 14.74908 THz, the remarkable “shadow”, which is much larger than the structure diameter, can be seen in both the forward and backward directions in Fig. 3(h), and the total magnetic field matches well with the scattering field shown in Fig. 3(g).

To facilitate the realization of the experiment and practical application, the effects of the material losses and the structural changes are analyzed in detail in Fig. 4. First, considering the optical losses of graphene, as shown in Fig. 4(a), the superscattering with resonantly overlapped multipoles still exists at corresponding resonant frequencies when changing the relaxation time τ , and the NSCs of corresponding resonance peaks are slightly reduced due to the addition of graphene’s losses. Then, to illustrate the high tolerance to structural design, the total scattering spectra are plotted in Fig. 4(b) by varying thickness d_1 of the innermost layer of the dielectric and the corresponding scattering spectra of $d_1 = 1400$ nm, $d_1 = 1500$ nm, and $d_1 = 1600$ nm are shown by the green, blue, and red solid curves, respectively. Except for d_1 , the other parameters are the same as those in the structure of Fig. 1(a). As the thickness d_1 increases gradually, though the positions of the resonant frequencies will

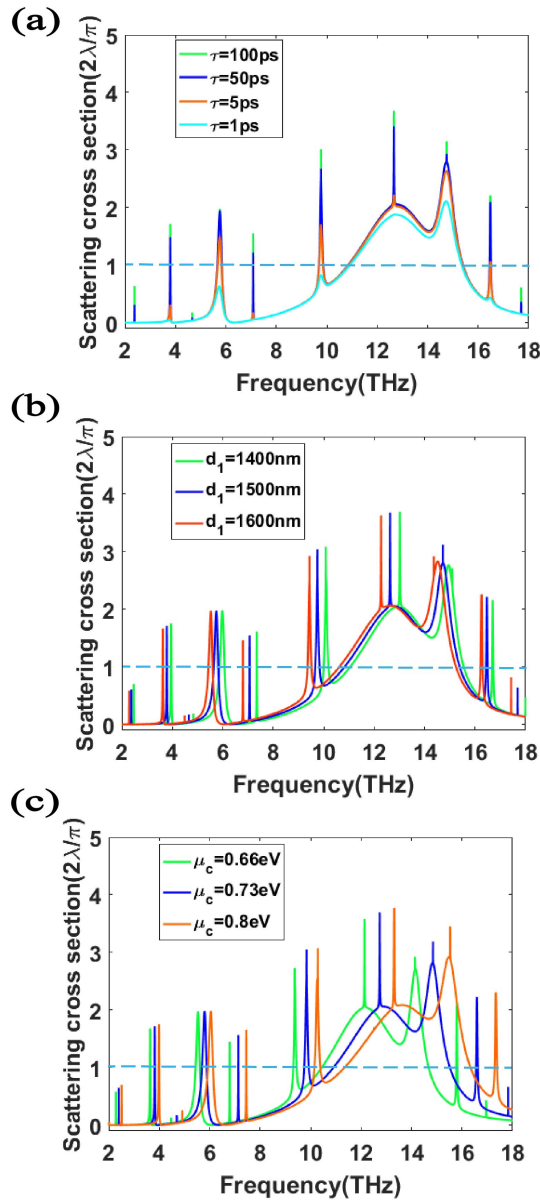


Fig. 4. (a) Influence of graphene's losses on multifrequency superscattering is shown through the total scattering spectra for different lossy cases. Except τ , other parameters are the same as those in the structure of Fig. 1(a). Influences of the thickness d_1 of the innermost layer of the dielectric and chemical potential μ_c of all graphene shells on multifrequency superscattering in the presence of graphene's losses are shown in (b) and (c), respectively. Except d_1 in (b) or μ_c in (c), other parameters are the same as those in the structure of Fig. 1(a).

move to the lower frequencies, superscattering with resonantly overlapped multipoles can still be obtained, and the NSCSs at the corresponding resonant frequencies are nearly unchanged. Compared with metal materials, graphene has the advantage of adjustability. Next, the tunability of graphene shells is illustrated by changing the chemical potential μ_c . The corresponding scattering spectra of $\mu_c = 0.66$ eV, $\mu_c = 0.73$ eV, and $\mu_c = 0.8$ eV are shown by the green, blue, and red solid curves in Fig. 4(c),

respectively. When the chemical potential increases, the positions of resonant frequencies will move towards the higher frequencies, and the superscattering phenomenon still exists with the NSCSs of corresponding resonance peaks almost unchanged. From Fig. 4, when considering the material losses and changing the structural parameters, superscattering with resonantly overlapped multipoles can be still obtained, which indicates that superscattering for a graphene-based subwavelength structure has a good tolerance to material losses and variations of structural parameters.

4. Conclusion

In conclusion, we propose that a graphene-based subwavelength structure can be a promising and versatile platform for the demonstration of simultaneous multifrequency superscattering and superscattering shaping with different engineered scattering patterns. Based on Bohr's model and dispersion engineering, it is further demonstrated that such efficient superscattering pattern shaping is induced by the interferences of multipoles resonantly overlapped. In contrast with multilayer plasmonic structures, the performance of the proposed structure can be easily refined for the desired frequency by adjusting the chemical potential and loss of the graphene layer. Owing to multiple polaritonic dispersion lines in a graphene-based subwavelength structure, the phenomena of multifrequency superscattering are found to have a high tolerance to some structural variations and realistic graphene loss. In addition, more exotic scattering phenomena are expected in such a platform, such as dynamically tunable multifrequency cloaking and other multifrequency scattering-based devices.

Acknowledgement

This work was supported by the National Natural Science Foundation of China (Nos. 11504306 and 92050102) and Fujian Provincial Natural Science Foundation (No. 2017J05015).

References

1. A. Kinkhabwala, Z. Yu, S. Fan, Y. Avlasevich, K. Müllen, and W. E. Moerner, "Large single-molecule fluorescence enhancements produced by a bowtie nanoantenna," *Nat. Photon.* **3**, 654 (2009).
2. S. Arslanagic and R. W. Ziolkowski, "Highly subwavelength, superdirective cylindrical nanoantenna," *Phys. Rev. Lett.* **120**, 237401 (2018).
3. C. Loo, A. Lowery, N. Halas, J. West, and R. Drezek, "Immunotargeted nano-shells for integrated cancer imaging and therapy," *Nano Lett.* **5**, 709 (2005).
4. J. Sheng, J. Xie, and J. Liu, "Multiple super-resolution imaging in the second band of gradient lattice spacing photonic crystal flat lens," *Chin. Opt. Lett.* **18**, 120501 (2020).
5. J. Zhao, X. Y. Zhang, C. R. Yonzon, A. J. Haes, and R. P. Van Duyne, "Localized surface plasmon resonance biosensors," *Nanomedicine* **1**, 219 (2006).
6. J. Wang, X. Wang, and M. Zeng, "Broadband transverse displacement sensing of silicon hollow nanodisk under focused radial polarization illumination in the near-infrared region," *Chin. Opt. Lett.* **18**, 063602 (2020).
7. A. Schliesser, N. Picqué, and T. W. Hänsch, "Mid-infrared frequency combs," *Nat. Photon.* **6**, 440 (2012).

8. M. A. Green and S. Pillai, "Harnessing plasmonics for solar cells," *Nat. Photon.* **6**, 130 (2012).
9. W. Xu, L. Xie, and Y. Ying, "Mechanisms and applications of terahertz metamaterial sensing: a review," *Nanoscale* **9**, 13864 (2017).
10. L. Novotny and B. Hecht, *Principles of Nano-optics*, 2nd ed. (Cambridge University, 2012).
11. Y. Zhai, Y. Ma, S. N. David, D. Zhao, R. Lou, G. Tan, R. Yang, and X. Yin, "Scalable-manufactured randomized glass-polymer hybrid metamaterial for daytime radiative cooling," *Science* **355**, 1062 (2017).
12. T. Yang, H. Chen, X. Luo, and H. Ma, "Superscatterer: enhancement of scattering with complementary media," *Opt. Express* **16**, 18545 (2008).
13. W. H. Wee and J. B. Pendry, "Shrinking optical devices," *New J. Phys.* **11**, 073033 (2009).
14. Z. Ruan and S. Fan, "Superscattering of light from subwavelength nanostructures," *Phys. Rev. Lett.* **105**, 013901 (2010).
15. R. J. Li, X. Lin, S. S. Lin, X. Liu, and H. S. Chen, "Tunable deep-subwavelength superscattering using graphene monolayers," *Opt. Lett.* **40**, 1651 (2015).
16. R. J. Li, X. Lin, S. S. Lin, X. Liu, and H. S. Chen, "Atomically thin spherical shell-shaped superscatterers based on Bohr model," *Nanotechnology* **26**, 505201 (2015).
17. R. Li, B. Zheng, X. Lin, R. Hao, S. Lin, W. Yin, E. Li, and H. Chen, "Design of ultracompact graphene-based superscatterers," *IEEE J. Sel. Top. Quantum Electron.* **23**, 4600208 (2017).
18. W. Liu, "Ultra-directional super-scattering of homogenous spherical particles with radial anisotropy," *Opt. Express* **23**, 14734 (2015).
19. W. Liu, B. Lei, J. Shi, and H. Hu, "Unidirectional superscattering by multilayered cavities of effective radial anisotropy," *Sci. Rep.* **6**, 34775 (2016).
20. W. Liu, "Superscattering pattern shaping for radially anisotropic nanowires," *Phys. Rev. A* **96**, 023854 (2017).
21. W. Wan, W. Zheng, Y. Chen, and Z. Liu, "From Fano-like interference to superscattering with a single metallic nanodisk," *Nanoscale* **6**, 9093 (2014).
22. Y. Huang and L. Gao, "Superscattering of light from core-shell nonlocal plasmonic nanoparticles," *J. Phys. Chem. C* **118**, 30170 (2014).
23. A. Mirzaei, A. Miroshnichenko, I. Shadrivov, and Y. Kivshar, "Superscattering of light optimized by a genetic algorithm," *Appl. Phys. Lett.* **105**, 011109 (2014).
24. C. Wang, C. Qian, H. Hu, L. Shen, Z. Wang, H. Wang, Z. Xu, B. Zhang, H. Chen, and X. Lin, "Superscattering of light in refractive-index near-zero environments," *Prog. Electromagn. Res.* **168**, 15 (2020).
25. M. Zhou, L. Shi, J. Zi, and Z. Yu, "Extraordinarily large optical cross section for localized single nanoresonator," *Phys. Rev. Lett.* **115**, 023903 (2015).
26. P. Del'Haye, T. Herr, E. Gavartin, M. Gorodetsky, R. Holzwarth, and T. J. Kippenberg, "Octave spanning tunable frequency comb from a microresonator," *Phys. Rev. Lett.* **107**, 063901 (2011).
27. F. C. Cruz, D. L. Maser, T. Johnson, G. Ycas, A. Klose, F. R. Giorgetta, I. Coddington, and S. A. Diddams, "Mid-infrared optical frequency combs based on difference frequency generation for molecular spectroscopy," *Opt. Express* **23**, 26814 (2015).
28. C. Qian, X. Lin, Y. Yang, F. Gao, Y. Shen, J. Lopez, I. Kaminer, B. Zhang, E. Li, M. Soljačić, and H. Chen, "Multifrequency superscattering from subwavelength hyperbolic structures," *ACS Photon.* **5**, 1506 (2018).
29. H. W. Wu, Y. Fang, J. Q. Quan, Y. Z. Han, Y. Q. Yin, Y. Li, and Z. Q. Sheng, "Multifrequency superscattering with high Q factors from a deep-subwavelength spoof plasmonic structure," *Phys. Rev. B* **100**, 235443 (2019).
30. C. Qian, X. Lin, Y. Yang, X. Xiong, H. Wang, E. Li, I. Kaminer, B. Zhang, and H. Chen, "Experimental observation of superscattering," *Phys. Rev. Lett.* **122**, 063901 (2019).
31. V. I. Shcherbinin, V. I. Fesenko, T. I. Tkachova, and V. R. Tuz, "Superscattering from subwavelength corrugated cylinders," *Phys. Rev. Appl.* **13**, 024081 (2020).
32. S. H. Raad, C. J. Zapata-Rodríguez, and Z. Atlasbaf, "Multi-frequency superscattering from sub-wavelength graphene-coated nanotubes," *J. Opt. Soc. Am. B* **36**, 2292 (2019).
33. R. Kumar and K. Kajilawa, "Superscattering from cylindrical hyperbolic metamaterials in the visible region," *Opt. Express* **28**, 1507 (2020).
34. R. Kumar and K. Kajikawa, "Comparison of cylinder- and planar-effective medium approximations on calculation of scattering properties of cylindrical hyperbolic metamaterials," *J. Opt. Soc. Am. B* **36**, 559 (2019).
35. J. Chai, P. Hu, L. Ge, H. Xiang, and D. Han, "Tunable terahertz cloaking and lasing by the optically pumped graphene wrapped on a dielectric cylinder," *J. Phys. Commun.* **3**, 035016 (2019).
36. W. Liu, A. E. Miroshnichenko, and Y. S. Kivshar, "Q-factor enhancement in all-dielectric anisotropic nanoresonators," *Phys. Rev. B* **94**, 195436 (2016).
37. K. Koshelev, A. Bogdanov, and Y. Kivshar, "Meta-optics and bound states in the continuum," *Sci. Bull.* **64**, 836 (2019).
38. T. Zhan, X. Shi, Y. Dai, X. Liu, and J. Zi, "Transfer matrix method for optics in graphene layers," *J. Phys. Condens. Matter.* **25**, 215301 (2013).
39. W. Liu and Y. S. Kivshar, "Generalized Kerker effects in nanophotonics and meta-optics," *Opt. Express* **26**, 13085 (2018).
40. W. Liu, "Generalized magnetic mirrors," *Phys. Rev. Lett.* **119**, 123902 (2017).
41. H. C. van de Hulst, *Light Scattering by Small Particles* (Dover, 1981).